nature portfolio

https://doi.org/10.1038/s41586-023-06745-7

Supplementary information

Low-loss contacts on textured substrates for inverted perovskite solar cells

In the format provided by the authors and unedited

Supplementary Information for:

Low-loss contacts on textured substrates for inverted perovskite solar cells

So Min Park,[1,4]† Mingyang Wei,[2]† Nikolaos Lempesis,[3]† Wenjin Yu,[5] Tareq Hossain,[6] Lorenzo Agosta,[3] Virginia Carnevali,[3] Harindi R. Atapattu,[6] Peter Serles,[7] Felix T. Eickemeyer,[2] Heejong Shin,[1] Maral Vafaie,[4] Deokjae Choi,[1] Kasra Darabi,[8] Eui Dae Jung,[4] Yi Yang,[1] Da Bin Kim,[4] Shaik M. Zakeeruddin,[2] Bin Chen,[1] Aram Amassian,[8] Tobin Filleter,[7] Mercouri G. Kanatzidis,[1] Kenneth R. Graham,[6] Lixin Xiao,[5] Ursula Rothlisberger,[3] Michael Grätzel[2]* & Edward H. Sargent[1,4,9]*

[1]Department of Chemistry, Northwestern University, Evanston, Illinois 60208, United States

[2]Laboratory of Photonics and Interfaces, Ecole Polytechnique Fédérale de Lausanne, Lausanne, 1015, Switzerland

[3]Laboratory of Computational Chemistry and Biochemistry, Ecole Polytechnique Fédérale de Lausanne, Lausanne, 1015, Switzerland

[4]Department of Electrical and Computer Engineering, University of Toronto, Toronto, Ontario, M5S 3G4, Canada

[5]State Key Laboratory for Artificial Microstructure and Mesoscopic Physics, Department of Physics, Peking University, Beijing 100871, P. R. China

[6]Department of Chemistry, University of Kentucky, Lexington, KY, 40506, United States

[7]Department of Mechanical and Industrial Engineering, University of Toronto, Toronto, Ontario, M5S 3G8, Canada

[8]Department of Materials Science and Engineering, and Organic and Carbon Electronics Laboratories (ORaCEL), North Carolina State University, Raleigh, NC, 27695, United States

[9]Department of Electrical and Computer Engineering, Northwestern University, Evanston, Illinois 60208, United States

† These authors contributed equally to this work.

* Corresponding authors: ted.sargent@northwestern.edu; michael.graetzel@epfl.ch

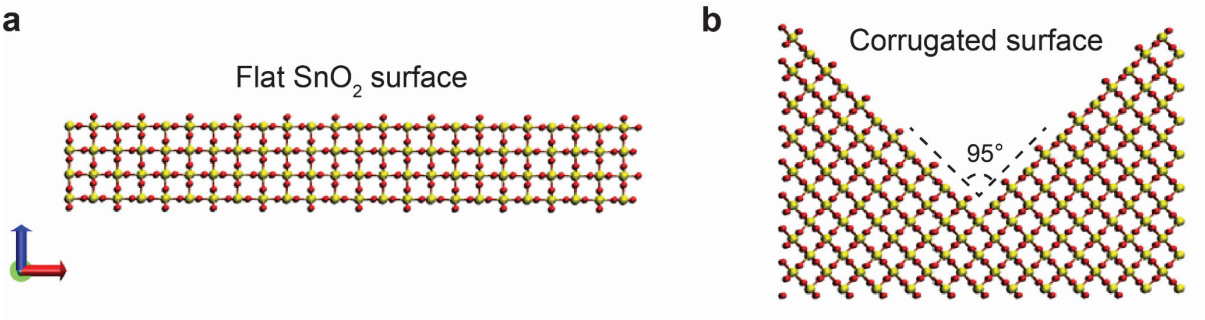

Supplementary Figure 1| a, b, Molecular representations of flat (**a**) and corrugated (**b**) SnO_2 (110) surfaces. For the corrugated surface, the angle between the two SnO_2 (110) crystallographic facets is 95°, comparable with the angle observed from TEM images of FTO substrates (Fig. 2d). The width of the V-shaped crevice was 6 nm. Sn and O atoms are represented by yellow and red spheres, respectively.

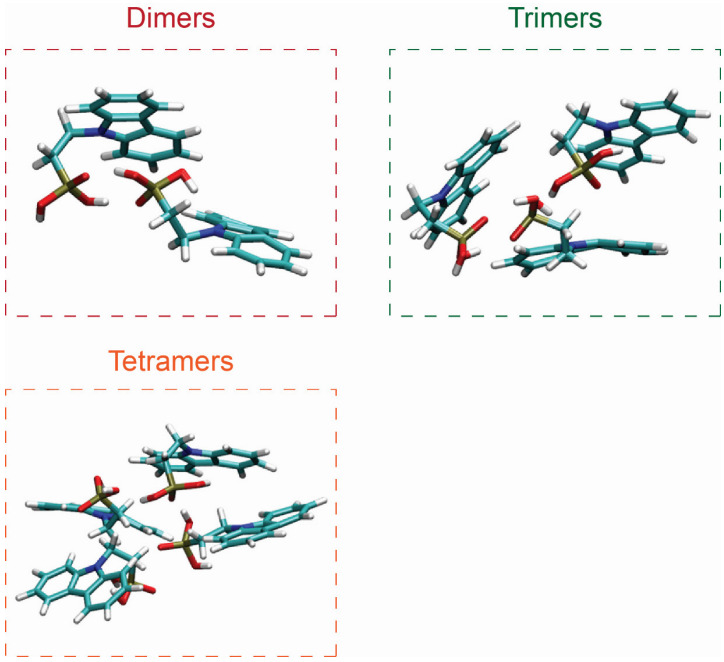

Supplementary Figure 2| Representative molecular conformations of various types of 2PACz clusters formed during classical MD simulations.

Supplementary Note 1

Effects of surface morphology on the cluster formation process

On flat surfaces, cluster formation is initially absent but becomes pronounced as the concentration of 2PACz increases (Supplementary Fig. 3). However, for textured surfaces, dimers were observed throughout the range of considered 2PACz concentrations (Supplementary Fig. 4). We ascribed this behavior to the inclined geometry of textured SnO_2 slabs, which confines spaces and thereby facilitates 2PACz molecules to approach one another and nucleate[1]. Correspondingly, when the system contains more than 80 2PACz molecules, there is a significant increase in the number of trimers and tetramers on textured surfaces. Interestingly, beyond this threshold concentration, the number of dimers remains practically constant, suggesting that besides forming new dimers, additional 2PACz molecules are added to existing ones to form higher-order clusters. This leads to the conclusion that the textured surface favors the formation of higher-order clusters at the expense of dimers.

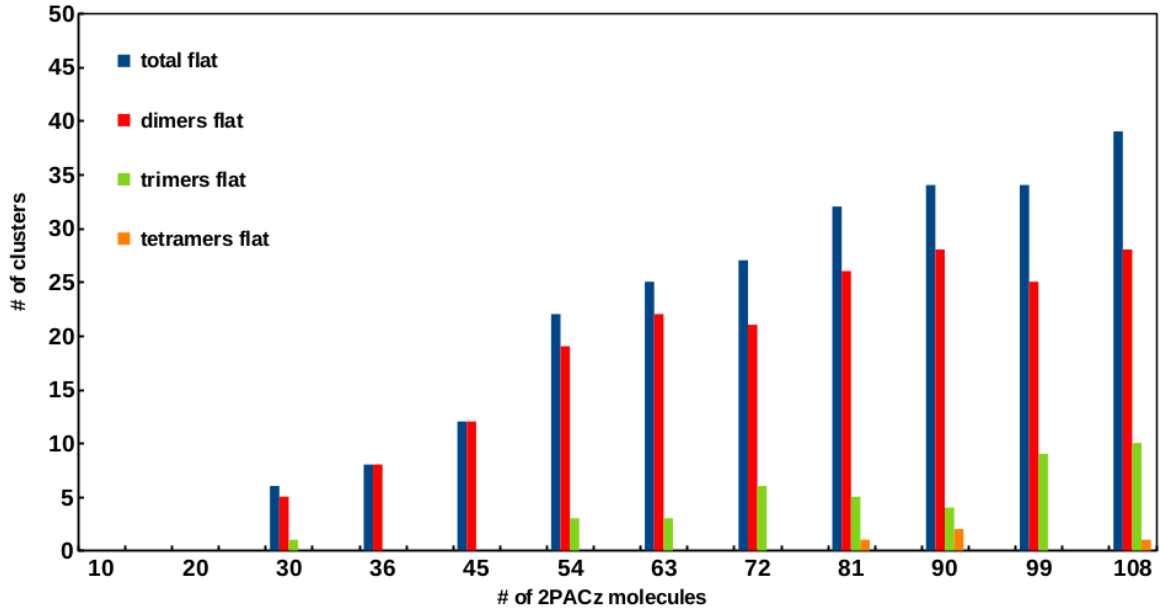

Supplementary Figure 3| Populations of types of clusters formed at different simulated 2PACz concentrations when added on a flat SnO_2 surface. The total number of clusters is shown in blue, while the populations of dimers, trimers, and tetramers are shown in red, green, and orange, respectively.

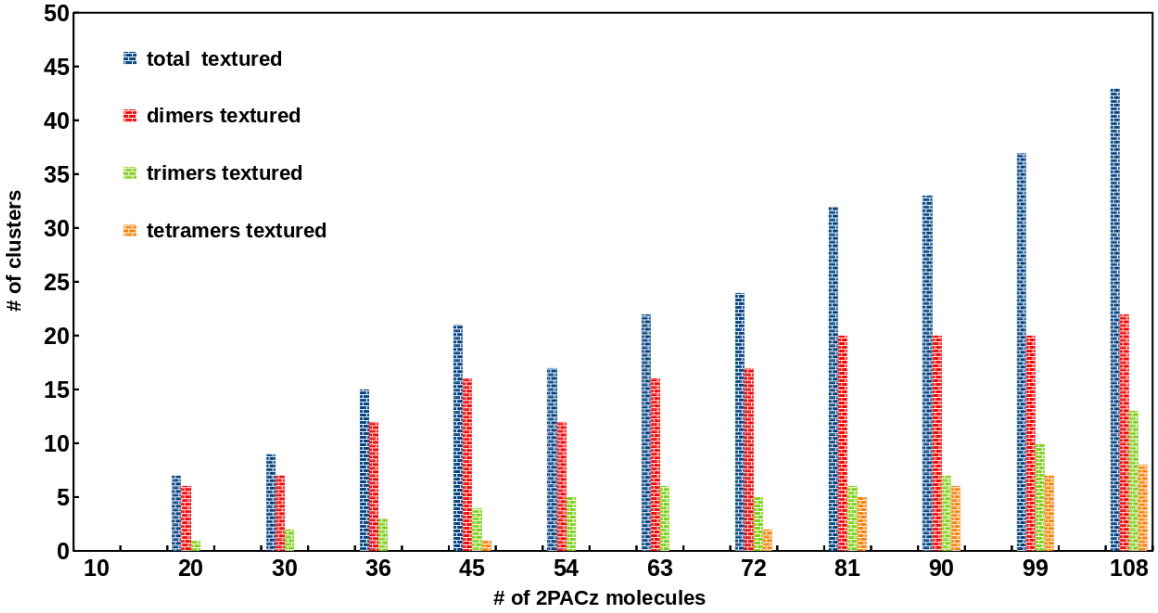

Supplementary Figure 4| Populations of types of clusters formed at different simulated 2PACz concentrations when added on a textured SnO_2 surface. The total number of clusters is shown in blue, while the populations of dimers, trimers, and tetramers are shown in red, green, and orange, respectively.

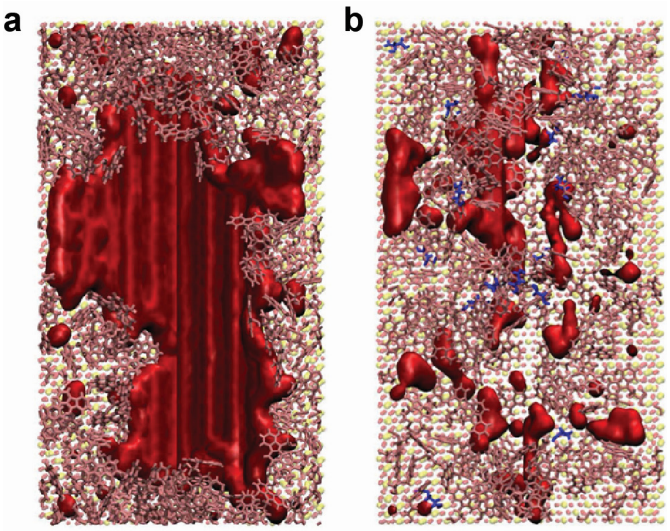

Supplementary Figure 5| Surface coverage of 2PACz and 3-MPA molecules. a,b, The SnO_2 free surface calculated for the cases without 3-MPA (**a**) and with 3-MPA (**b**). Red clouds visualize the extent of the free surface area not covered by either 2PACz or 3-MPA molecules.

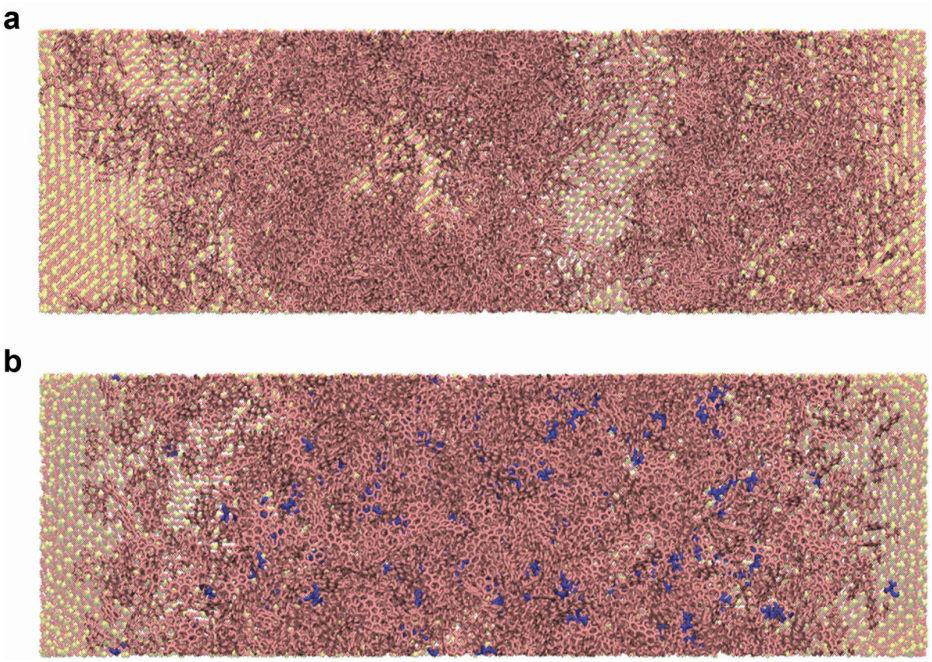

Supplementary Figure 6| MD of phosphonic acid adsorption with a 22-nm-wide simulation box. a, b, Top views of equilibrated molecular representations of control (**a**) and mixed (**b**) systems. 2PACz and 3-MPA (where applicable) are shown in pink and blue, respectively; Sn and O atoms, shown in the background, are depicted in yellow and red, respectively.

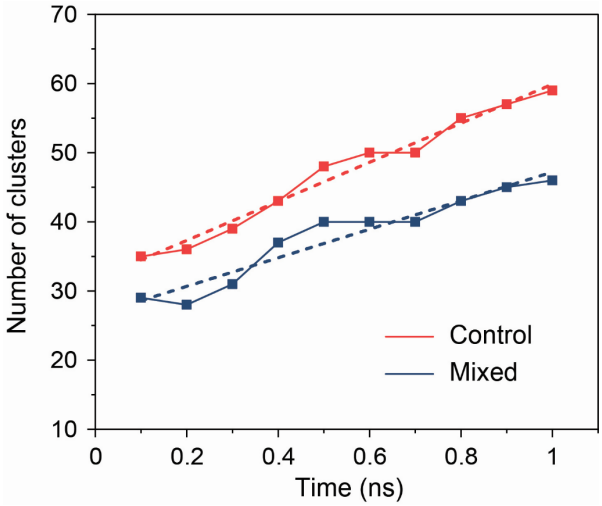

Supplementary Figure 7| 2PACz cluster formation dynamics within the initial 1 ns of classical MD simulations. The rate of cluster formation is expressed by the slope of linear fits (dashed lines) for the control (28 ns^{-1}) and mixed (20 ns^{-1}) systems. The incorporation of 3-MPA leads to a decrease in both the rate of cluster formation and the total number of clusters.

Supplementary Note 2

Atomic-level adsorption mechanism of 2PACz molecules

We performed AIMD simulations at 300 K and 1 atm. Both 2PACz and 3-MPA molecules underwent deprotonation after adsorption on the SnO_2 (110) (Supplementary Fig. 8). Immediately thereafter, they exhibited strong binding to the surface without any further noticeable diffusion. We set up a simulation with six 2PACz molecules and one 3-MPA molecule initially placed at a certain distance from the SnO_2 surface. The detailed interaction between 2PACz and 3-MPA is depicted in Movie S3. The thiol group of 3-MPA establishes a hydrogen bond with the phosphonic acid group of 2PACz. This resultant supramolecular structure mitigates the formation of higher-order clusters by restricting the interaction with nearby 2PACz molecules (Fig. 1f). As these two molecules reach the SnO_2 surface, the 2PACz-SnO_2 and the 3-MPA-SnO_2 interactions become dominant over their intermolecular attractions. Correspondingly, both molecules undergo deprotonation and adsorb onto the surface. It is noted that 3-MPA can adopt a temporary standing adsorption mode, with the carboxylate group bound to the surface and the thiol group protruding away from it, which can help guiding other freely diffusing 2PACz molecules to the surface.

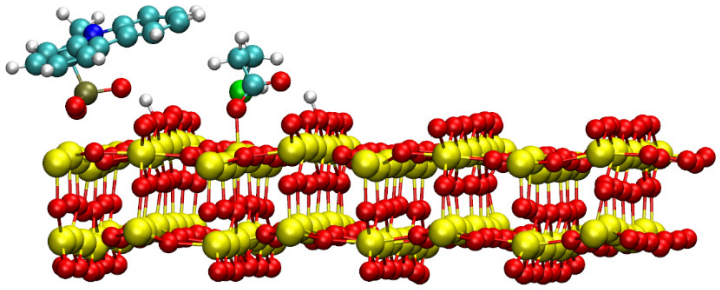

Supplementary Figure 8| Snapshot of an AIMD simulation showing the deprotonation of the phosphonic acid group of 2PACz and the carboxyl group of 3-MPA on SnO_2 (110). Sn, O, C, H, P, N, and S atoms are shown in yellow, red, cyan, white, tan, blue, and green, respectively.

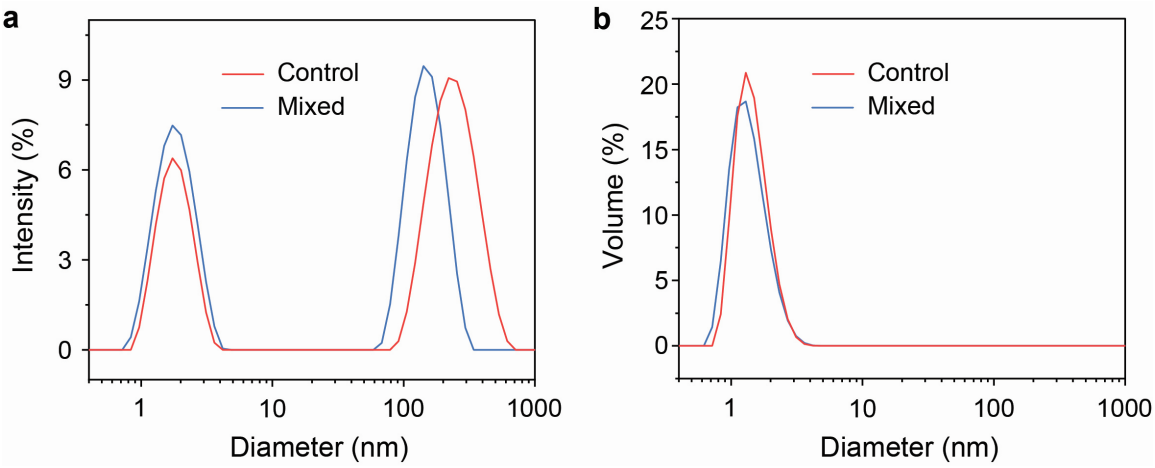

Supplementary Figure 9| DLS particle size distributions in SAM-processing solutions. a, b, Intensity-weighted (**a**) and volume-weighted (**b**) distributions of 2PACz (control) or 2PACz:3-MPA (in a molar ratio of 9:1) (mixed) in anhydrous ethanol (1 mM) solution. The 2PACz micelles were observed in intensity-weighted distributions, showing an average hydrodynamic diameter of 250 nm and 150 nm for the control and mixed solutions, respectively.

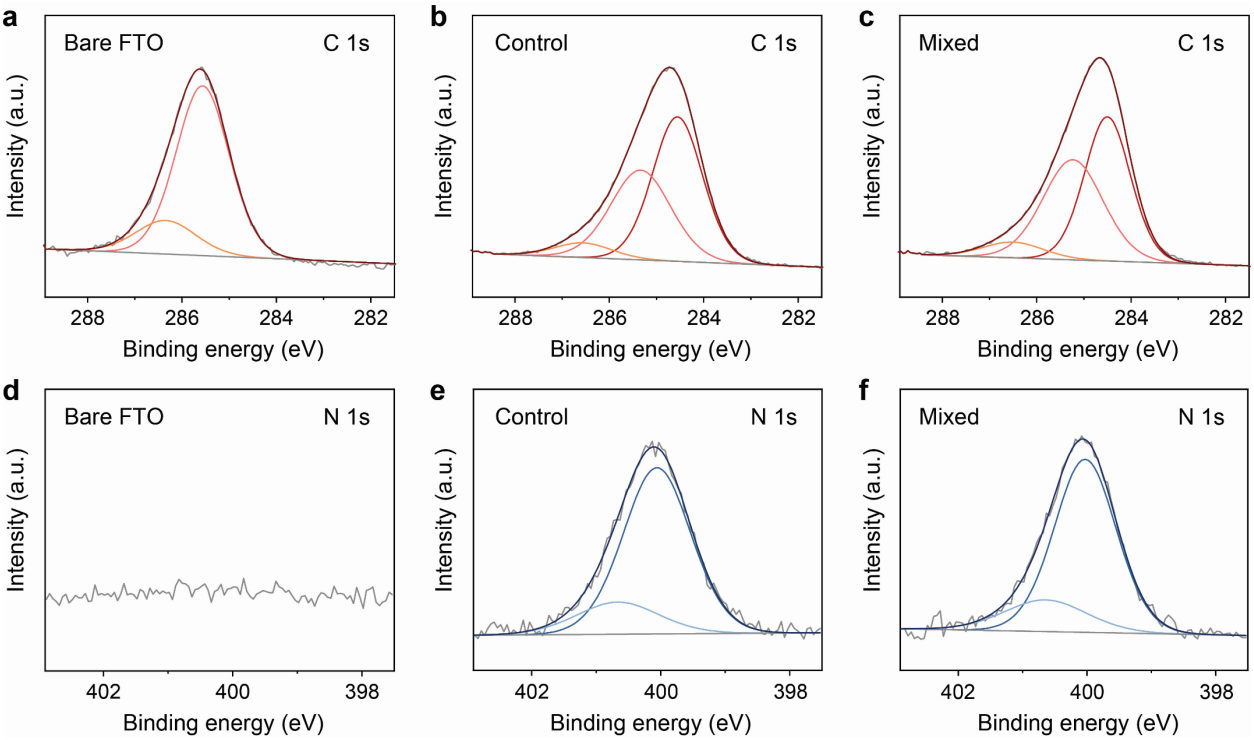

Supplementary Figure 10| XPS spectra of bare and SAM-modified FTO substrates. a-c, C 1s region of bare FTO (**a**), control (**b**) and (**c**) mixed SAM deposited substrates. The dark red line represents a fit to the raw data. The red peak fits the C–C and C–H bonds and the pink peak to the C–N. The orange peak is attributed to C–OH/C–O–C contaminations for bare FTO and to C–P and C–OH/C–O–C contaminations for SAM deposited substrates[2]. **d-f,** N 1s region of bare FTO (**d**), control (**e**) and (**f**) mixed SAM deposited substrates. The dark blue line represents a fit to the raw data. The cyan peak, observed in thermally evaporated 2PACz films as well[3], might be attributed to impurities. The blue peak fits the N from carbazole.

Supplementary Note 3

Simulated vibrational power spectra and 2PACz/SnO_2 interactions

Supplementary Fig. 11 depicted the simulated vibrational power spectra of a 2PACz molecule adsorbed on the SnO_2 surface. These were calculated from the Fourier transform of the autocorrelation function of atomic velocities along the ab-initio MD trajectory (33 ps). We focused on two scenarios: (1) an isolated 2PACz molecule anchored to the surface and (2) a 2PACz molecule neighbouring with an adsorbed 3-MPA molecule. In both cases we calculated and extracted the vibrational components of the PO_3^{2-} group involved in the 2PACz adsorption. When the 3-MPA molecule is present, a red-shift of about 6 cm^{-1} was observed in the simulated spectrum.

The interactions between 2PACz and SnO_2 were illustrated in Supplementary Fig. 12. In the isolated scenario, the PO_3^{2-} group engages in bidentate binding by attaching its two oxygen atoms to surface Sn atoms, while the third oxygen weakly interacts with the transferred proton (Supplementary Fig. 12a). When a 2PACz molecule is situated next to an adsorbed 3-MPA molecule, the 3-MPA releases its COOH proton onto the bridging oxygen atom, thereby limiting the available deprotonation sites for the 2PACz molecule. As a result, in addition to the usual bidentate binding, the unreleased proton of 2PACz establishes a stable hydrogen bond with an adjacent bridging oxygen atom (Supplementary Fig. 12b). Based on these findings, we associated the red shift observed in the vibrational spectra (both experimentally and computationally) with the enhanced adsorption mode prompted by the presence of the 3-MPA molecule.

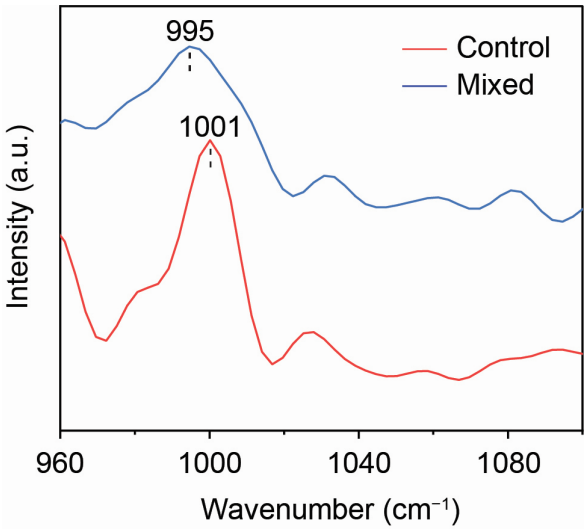

Supplementary Figure 11| Simulated vibrational power spectra of 2PACz with (mixed) and without (control) the presence of an MPA molecule on an adjacent SnO_2 adsorption site. The presence of the MPA molecule enhances the adsorption of the 2PCAz molecule, corroborated by a 6 cm^{-1} red-shift in the PO_3^{2-} vibrational mode.

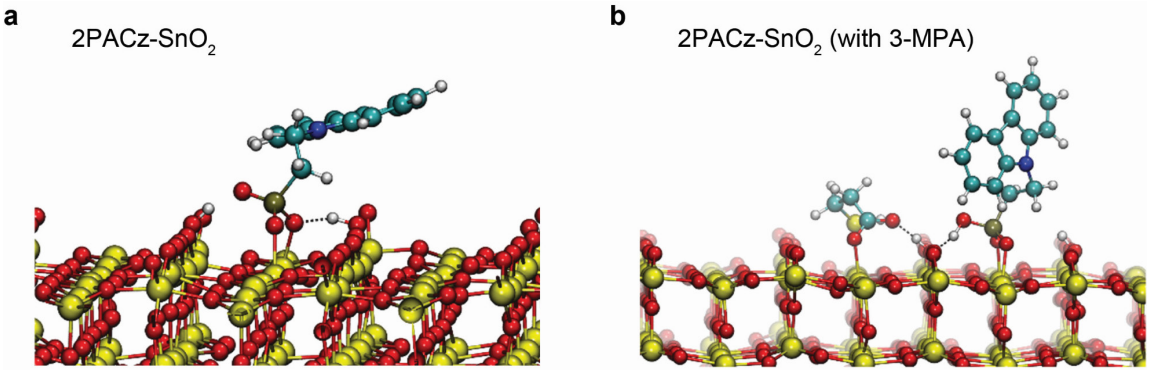

Supplementary Figure 12| Snapshots of AIMD simulations showing interactions between the 2PACz molecule and SnO_2 (110) surface. a,b, An isolated 2PACz molecule (**a**) and a 2PACz molecule with an adjacent 3-MPA molecule (**b**) adsorbed on the SnO_2 (110) surface after deprotonation. Sn, O, C, H, P, and N atoms are shown in yellow, red, cyan, white, tan, and blue, respectively.

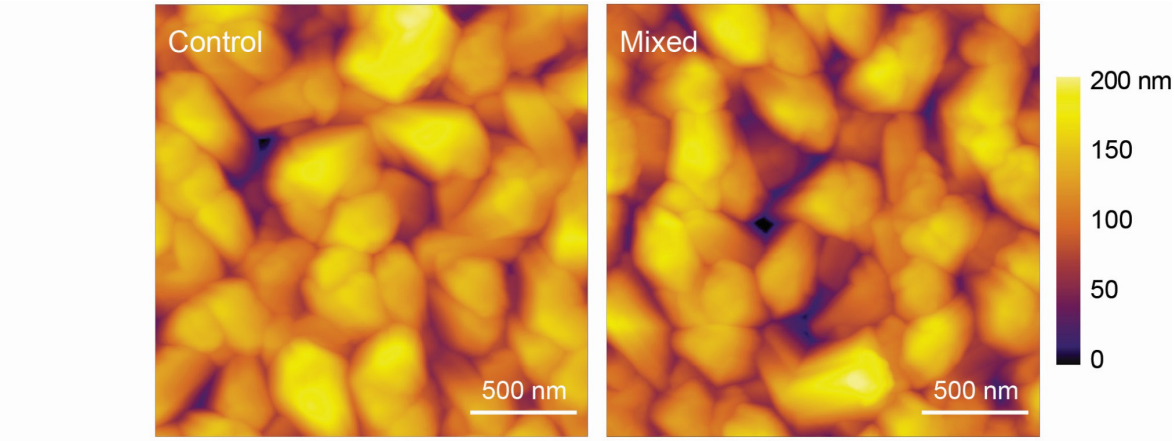

Supplementary Figure 13| Topography KPFM images of control (left) and mixed (right) SAM-coated FTO substrates.

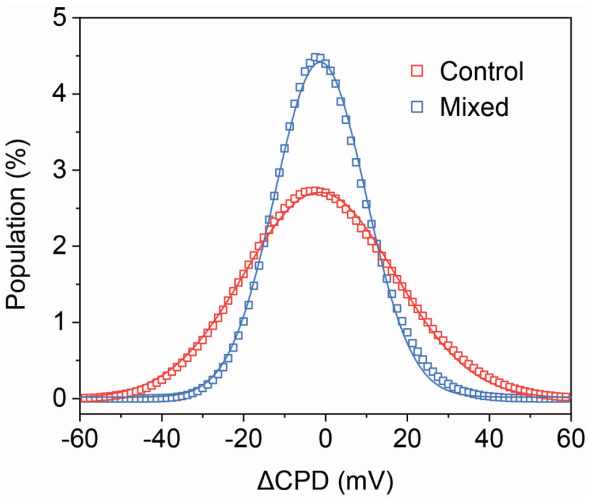

Supplementary Figure 14| Statistical histograms extracted from ΔCPD maps of control and mixed samples. Solid lines indicate Gaussian fits.

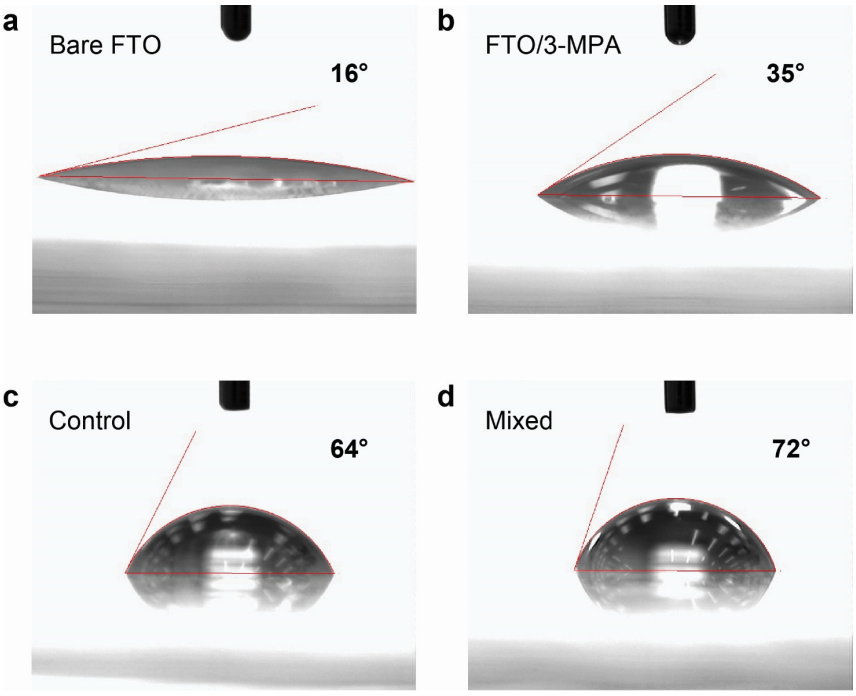

Supplementary Figure 15| Contact angle images of bare and SAM-coated FTO substrates. **a-d,** Images of the water droplet for bare (**a**), 3-MPA (**b**), 2PACz (control) (**c**), and 2PACz:3-MPA (mixed) (**d**) treated FTO substrates.

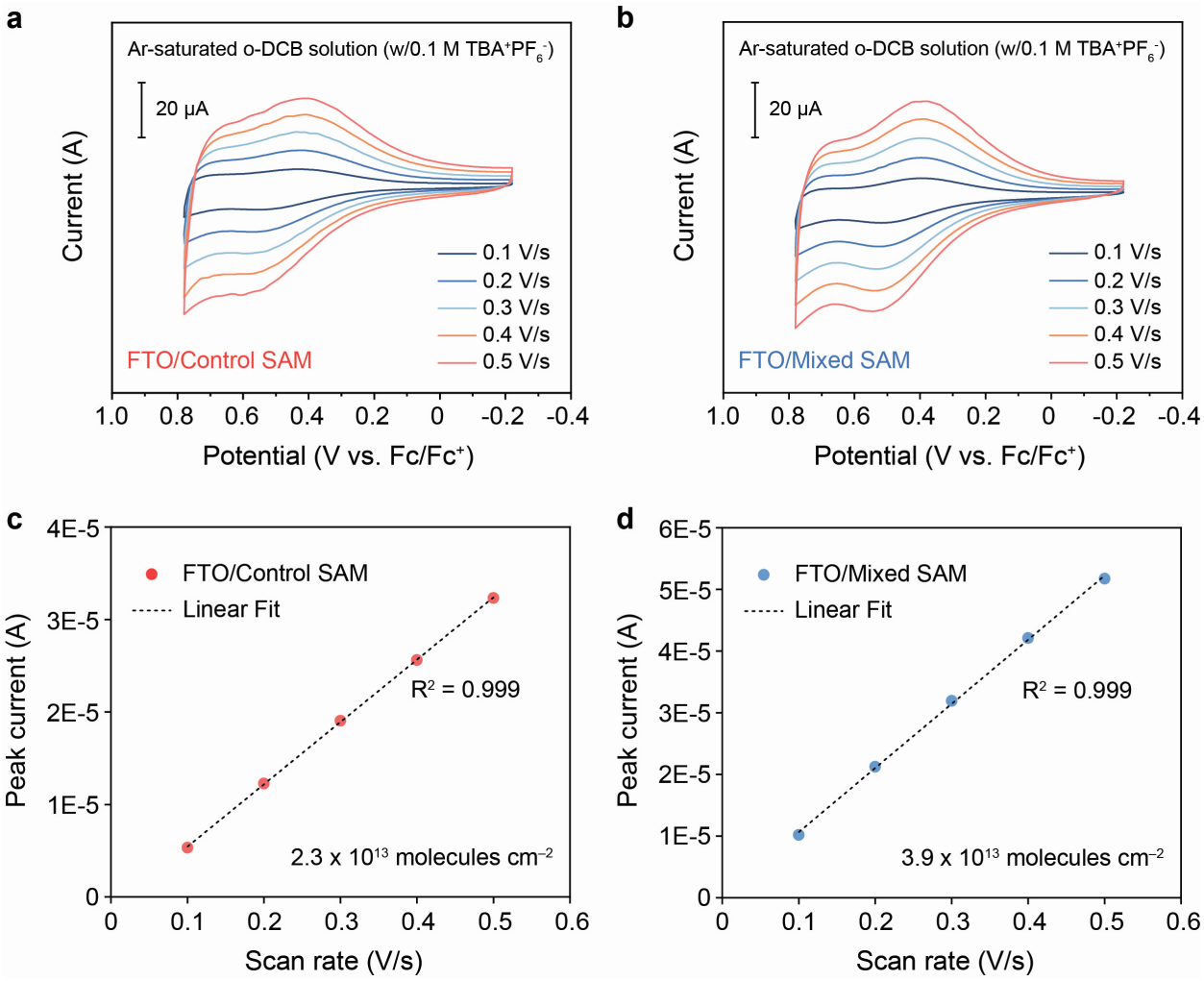

Supplementary Figure 16| Cyclic voltammetry measurements using SAM-coated FTO substrates as the working electrode. a,b, Cyclic voltammograms of control SAM (**a**) and mixed SAM (**b**) coated FTO substrates measured in Ar-saturated o-DCB solution under different voltage scan rates. **c,d,** The relationship between the oxidative peak current and the voltage scan rate for control (**c**) and mixed SAM (**d**) samples. The dashed line represents a linear fit to the raw data.

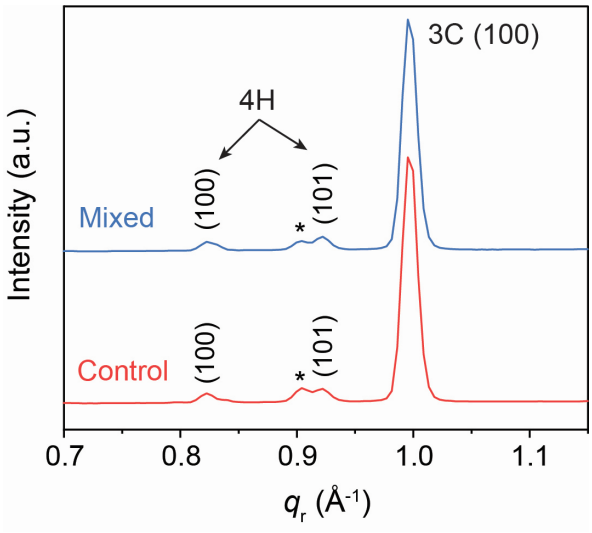

Supplementary Figure 17| Azimuthally integrated GIWAXS profiles of perovskite films deposited on control and mixed SAM-coated FTO substrates. The asterisk symbol indicates the PbI_2 phase.

Supplementary Table 1| Summary of PL peak position, PLQY, E_g, QFLS, and ΔV_{oc} for the perovskite thin films deposited on different substrates. $\Delta V_{oc} = (E_g - \text{QFLS})/q$, where q is elementary charge.

Substrates	Sample No.	PLQY (%)	E_g (eV)	QFLS (eV)	ΔV_{oc} (V)
Bare FTO	1	0.14	1.547	1.105	0.441
	2	0.15	1.547	1.109	0.439
	3	0.10	1.547	1.097	0.450
	4	0.13	1.550	1.107	0.443
	Average	0.13	1.548	1.105	0.443
Control SAM	1	8.0	1.551	1.213	0.337
	2	6.9	1.551	1.210	0.341
	3	6.8	1.546	1.205	0.341
	4	3.2	1.551	1.190	0.361
	5	8.5	1.551	1.215	0.336
	Average	6.7	1.550	1.207	0.343
Mixed SAM	1	9.1	1.545	1.211	0.334
	2	11.8	1.543	1.217	0.327
	3	11.0	1.544	1.215	0.329
	4	9.0	1.551	1.216	0.334
	5	9.7	1.544	1.212	0.332
	Average	10.1	1.546	1.214	0.331

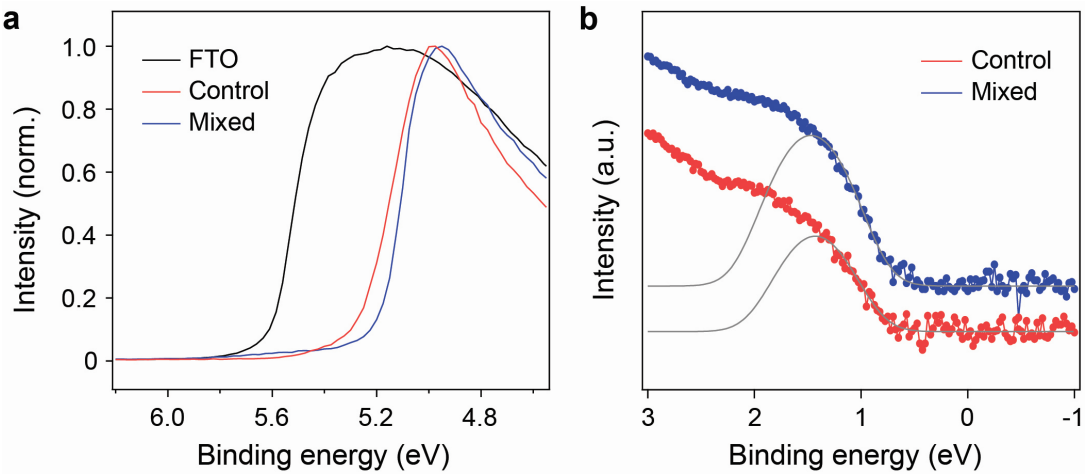

Supplementary Figure 18| a, UPS secondary electron cut-off region of bare FTO, control and mixed SAM deposited substrates. **b,** UPS valence band onset region plotted on a relative logarithmic scale of control and mixed SAM deposited substrates. The x-axis energy scale is with respect to the Fermi energy. Gaussian fit (grey solid line) was used to determine the valence band[4]. A Gaussian fit is used here to maintain consistency with the method used to define the IE of the perovskite.

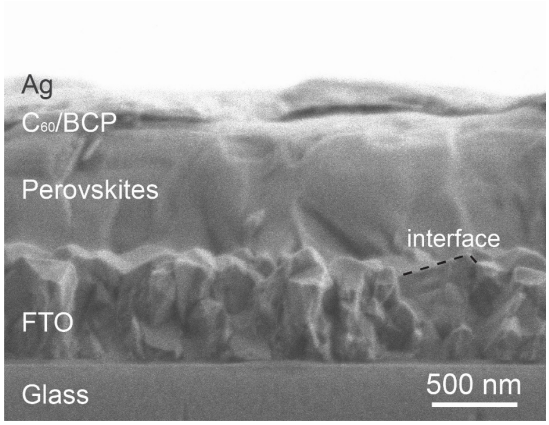

Supplementary Figure 19| Cross-sectional SEM image of the inverted PSC with the mixed SAM.

Supplementary Note 4

The origin of PCE improvements

From PL (Supplementary Table 1), we see that reduced interfacial recombination with the mixed SAM led to an increase in V_{oc} by ~10 mV. An additional V_{oc} improvement is attributed to a larger built-in field, as indicated by the VL shift from UPS measurements (Fig. 3j). This enhanced driving force also explains the higher FF of mixed-SAM-based devices. The random textures of FTO substrates helped to reduce light reflection losses within PSCs, yielding a maximum EQE of 98% at 550 nm (Fig. 4c). The integrated J_{sc} accounts for 95% of the Shockley-Queisser-limited photocurrent (27.05 mA cm^{-2}).

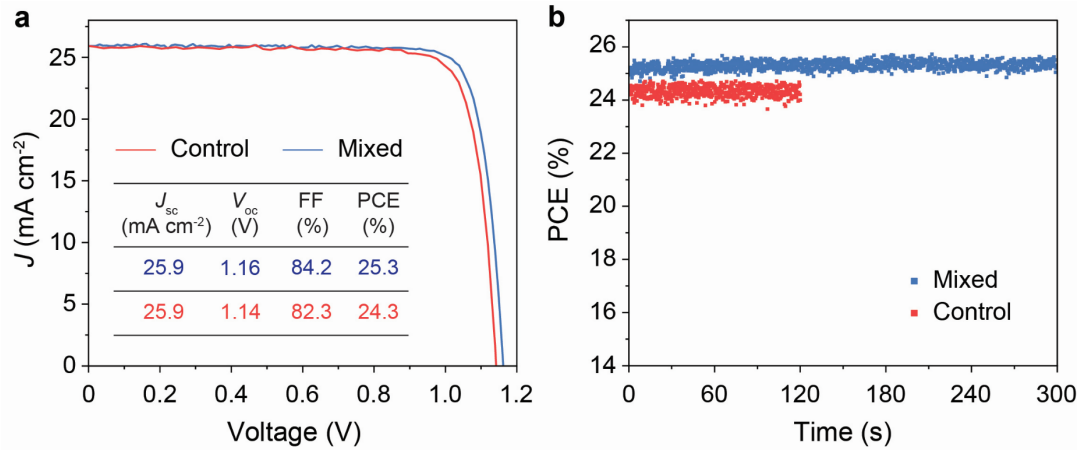

Supplementary Figure 20| Device performance of champion PSCs. a, J-V curves, and figures of merit of champion control and mixed SAM-based cells. **b,** Steady-state PCE output at a constant bias of 0.977 V and 1.019 V for control and mixed SAM-based PSCs, respectively.

mks Newport™	ACCREDITED Calibration Cert. # 2893.01	Technology and Application Center **PV Lab** Newport Calibration Cert. # 2691

DUT S/N: 729632 D4
Newport Calibration #: 2691
Manufacturer: University of Toronto
Material (single junction): Perovskite
Measurement Date: 12-Jan-2023
Temperature Sensor: TC-K, DUT Temperature: 25.0 ± 0.7 °C
Environmental conditions at the time of calibration: Temperature: 24 ± 3 °C; Humidity: 30 ± 20 %

The above DUT has been tested using the following methods to meet the ISO 17025 Standard by the PV Lab at Newport Corporation. Quoted uncertainties are expanded using a coverage factor of $k = 2$ and expressed with an approximately 95% level of confidence. Measurement of total irradiance is traceable to the World Radiometric Reference (WRR) and all other measurements and uncertainties are traceable to NIST and the International System of Units (SI). The performance parameters reported in this certificate apply only at the time of the test, and do not imply future performance.

***Designated area as defined by thin metal aperture mask.**

†Reported performance parameters were measured under a 10-point IV sweep configuration wherein the bias voltage (current for Voc determination) is held constant until the measured current (voltage for Voc) is determined to be unchanging at the 0.07% level. This is intended to represent the quasi-steady-state performance of the device. Total IV measurement time under these conditions was approximately 6 minutes.

Efficiency [%]	24.78†	±	0.79	V_oc [V]	1.1496	±	0.0088	I_sc [A]	0.001258	±	0.000027
P_max [mW]	1.223	±	0.036	V_max [V]	1.015	±	0.014	I_max [A]	0.001205	±	0.000027
FF [%]	84.5	±	1.6	Area [cm²]	0.04935*	±	0.00036	M	1.019	±	0.015

Methods:

I-V: ASTM E948-16 *Standard Test Method for Electrical Performance of Photovoltaic Cells Using Reference Cells Under Simulated Sunlight*
QE: ASTM E1021-15 *Standard Test Method for Spectral Responsivity Measurements of Photovoltaic Devices*

Standard Reporting Conditions:

Spectrum: AM1.5-G (ASTM G173-03/IEC 60904-3 ed. 2)
1000.0 W/m ² at 25.0°C

Secondary Reference Cell:

Device S/N: PVM 746
Device Material: GaAs
Window Material: BK7
Certification: National Renewable Energy Laboratory
A2LA accreditation certificate # 2236.01
ISO Tracking #: 2035
Certified short circuit current (I_{sc}) under standard reporting conditions (SRC): 105.87 mA
Calibration due date: 23-Apr-23

Solar Simulator:

Spectrum: Newport Corporation filename *Sol3A_Spectroradiometer_Scan_0230.xls*
Total irradiance: 1000 W/m² based on I_{sc} of the above Secondary Reference Cell

Quantum Efficiency for DUT:

Newport Corporation filename *QE 7299632 D4, 0,23 mA WLB.log*
Spectral mismatch correction factor: M = 1.019 ± 0.015

DUT Calibration Procedures:

Newport Corporation document WI1 (EQE).docx
Newport Corporation document Area Measurement WI2 (Area).docx
Newport Corporation document WI3 (IV.Sweep).docx

Supplementary Figure 21| Certified results of the inverted PSC with the mixed SAM.

Supplementary Table 2| Summary of certified PV parameters of >22% and >24% PCE inverted PSCs measured under the quasi-steady-state (QSS) and maximum power point (MPP) conditions, respectively.

V_{oc} (V)	J_{sc} (mA cm^{-2})	FF (%)	*J-V* PCE (%)	Stabilized PCE (%)	Conditions	Ref.
1.1496	**25.50**	**84.5**	**N.A.**	**24.78%**	**QSS (Newport)**	**This work**
1.1595	25.02	83.05	N.A.	24.09%	QSS (NREL)	S. M. Park, Science (2023)[5]
1.1607	25.44	81.48	N.A.	24.05%	QSS (NREL)	Q. Jiang, Nature (2022)[6]
1.1505	24.90	83.46	N.A.	23.91%	QSS (NREL)	H. Chen, Nat. Photonics (2022)[7]
1.1687	22.89	84.55	N.A.	22.62%	QSS (NREL)	S. Chen, Sci. Adv (2021)[8]
1.1429	23.84	82.0	N.A.	22.34%	QSS (Newport)	X. Zheng, Nat. Energy (2020)[9]
1.203	25.02	82.73	24.90%	24.71%	MPP (NPVM)	W.Peng, Science (2023)[10]
1.171	25.33	82.60	24.50%	24.25%	MPP (NPVM)	X. Wu, Adv. Mater. (2023)[11]
1.19	24.45	84.2	24.5%	24.1%	MPP (JET)	F. Li, Nat. Photonics (2023)[12]

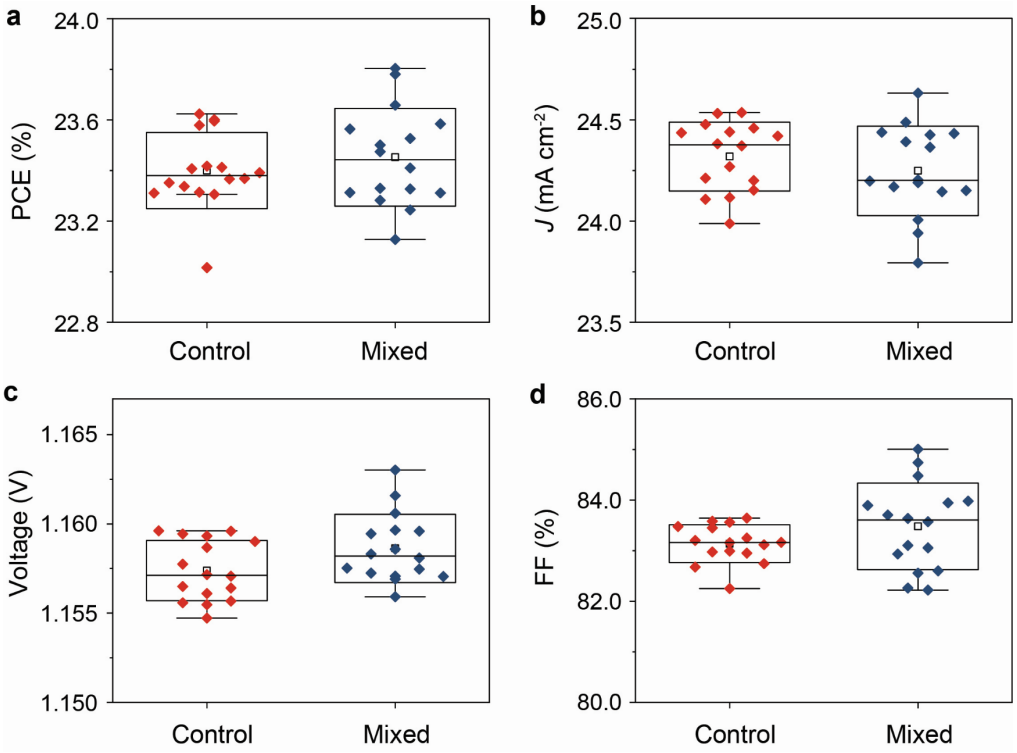

Supplementary Figure 22| PV parameters of ITO devices. a-d, PCE (**a**), J_{sc} (**b**), V_{oc} (**c**), and FF (**d**) of control and mixed SAM-coated devices (16 devices for each condition). Statistical distribution is represented in box-and-whisker plots (line within the box: median, box limit: standard deviation, whiskers: 1.5 outliers).

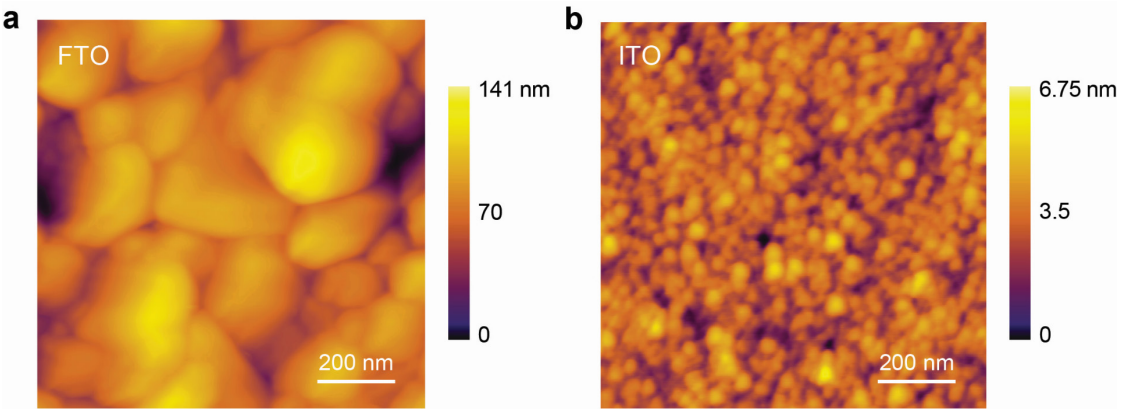

Supplementary Figure 23| a,b, Topography AFM images of bare FTO (**a**) and ITO (**b**) substrates. The areal surface roughness is 24 nm and 0.6 nm for FTO and ITO substrates, respectively.

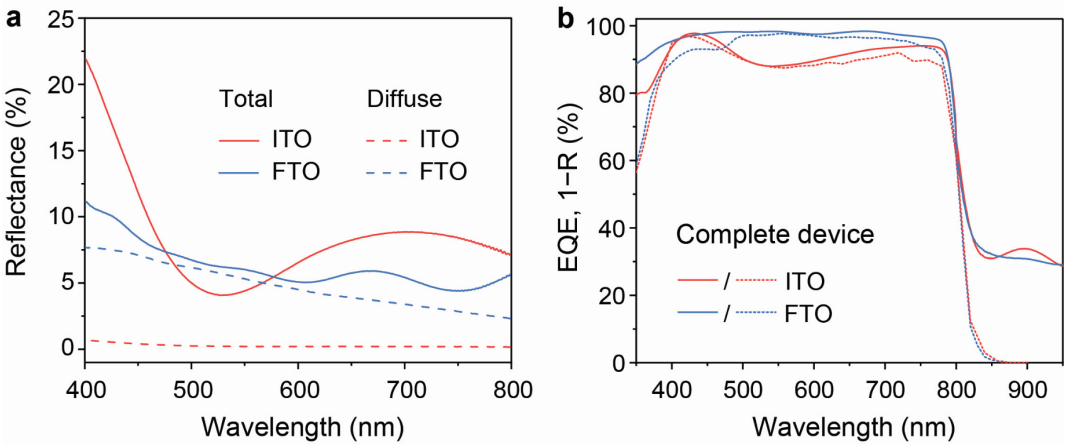

Supplementary Figure 24| Optical measurements of TCO substrates and complete devices. **a,** Total (solid line) and diffuse (dashed line) reflectance of bare ITO and FTO substrates. **b,** EQE and total absorptance (1-R) curves of complete ITO and FTO devices. The EQE curve of the FTO device has been presented in Fig. 4c.

Supplementary Note 5

Anchoring patterns of 2PACz and 3-MPA on ITO surfaces

To elucidate the adsorption behaviours of 2PACz and 3-MPA on ITO surfaces, we performed AIMD simulations of a 2PACz or 3-MPA molecule interacting with an ITO (111) surface (with 14 mol% Sn doping). The resultant adsorption configurations were shown in Supplementary Fig. 25. We found that the anchoring pattern of 2PACz on the ITO (111) surface mirrors that on the SnO_2 (110) surface, where the phosphonic acid group transfers two protons to the surface oxygen atoms and attaches its oxygen atoms to the surface indium atoms. The binding energy of −3.2 eV also aligns with that on the SnO_2 (110) surface (−3.2 eV). Conversely, the 3-MPA molecule binds via the −SH group, yet its COOH group remains inert, showing neither adsorption nor deprotonation on the ITO (111) surface. The binding energy for this pattern is −0.95 eV, distinct from the −2.6 eV calculated for the SnO_2 (110) configuration. The weaker adsorption of the 3-MPA molecule indicates a reduced anti-aggregation capability, as it could stay solvated rather than adhere to the ITO surface.

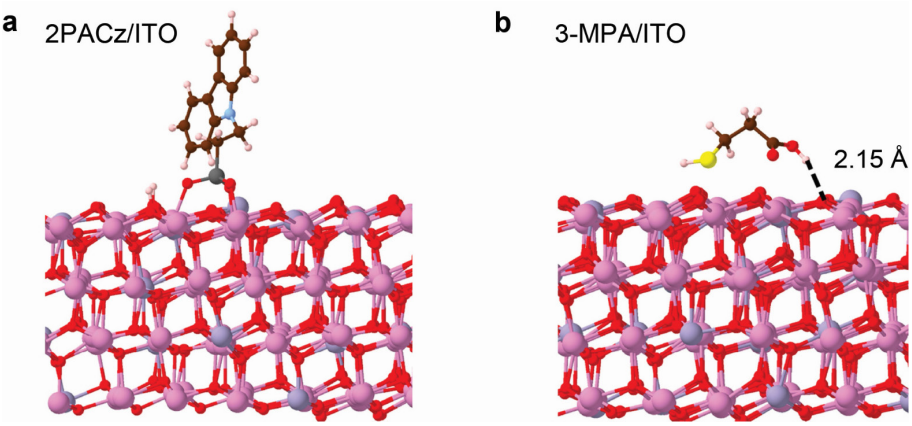

Supplementary Figure 25| Snapshots of AIMD simulations of 2PACz/ITO and 3-MPA/ITO interactions. a, b, 2PACz (**a**) and 3-MPA (**b**) molecules adsorbed on the ITO (111) surface. Colour legend: O red, H white, C brown, S yellow, In magenta, Sn grey, P dark grey.

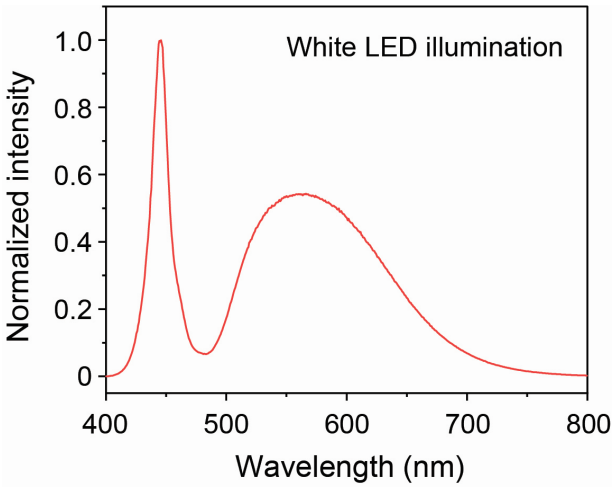

Supplementary Figure 26| Spectrum of the white LEDs, Bridgelux Vero 29 Array Series (https://www.bridgelux.com/products/vero-series#specifications), used for operating stability measurements. This light source does not contain UV components in its spectral range and exhibits a correlated colour temperature (CCT) of 5000 K.

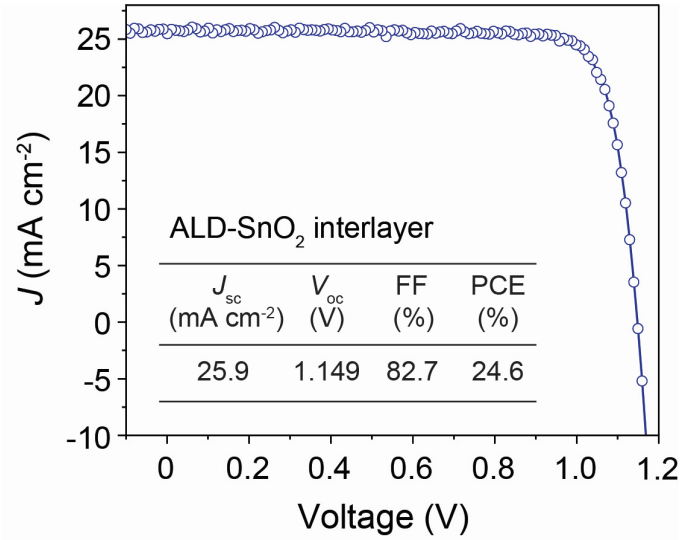

Supplementary Figure 27| J-V curve and figures of merit for the device used in stability testing. The device architecture is FTO/mixed SAM/Perovskite/C_{60}/ALD-SnO_2/Ag.

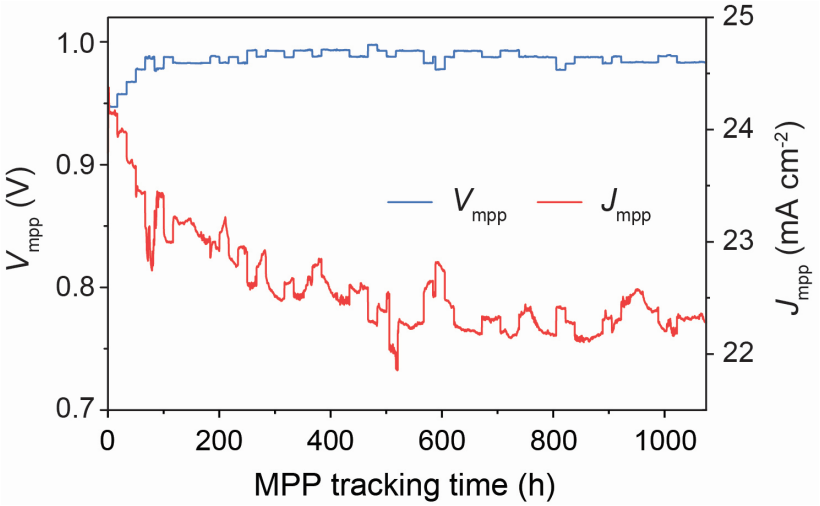

Supplementary Figure 28| J_{MPP} and V_{MPP} of the encapsulated mixed SAM device during 1075 h of continuous maximum-power-point tracking under 1-sun illumination at 65°C and 50% relative humidity.

Supplementary Table 3| Summary of reported device operating stability based on ISOS-L-3 protocols. RT = room temperature.

Light source	T	Environment	PCE @RT	PCE @high-T	Lifetime	Ref.
White LED	**65°C**	**~50% RH**	**24.6%**	**23.1% (65°C)**	**T_{95} = 1075 h**	**This work**
N.A.	65°C	~85% RH	25.0%	23.35% (65°C)	T_{82} = 500 h	P. Shi, Nature (2023)[13]
White LED	85°C	~50% RH	21.1%	19.9% (85°C)	T_{85} = 1560 h	S. M. Park, Science (2023)[5]
White LED	65°C	~50% RH	23.1%	N.A.	T_{92} = 500 h	H. Chen, Nat. Photonics (2022)[7]
Metal-halide lamp	85°C	~65% RH	17.4%	~16.5% (85°C)	T_{85} = 4000 h	X. Zhao, Science (2022)[14]
Xenon lamp	85°C	~50% RH	20.1%	~14.2% (85°C)	T_{95} = 1200 h	Y-H. Lin, Science (2020)[15]
Plasma lamp	65°C	~60% RH	21.1%	~19.5% (65°C)	$T_{96.8}$ = 1200 h	S. Yang, Science (2019)[16]

Supplementary References

1. Curcio, E., Curcio, V., Profio, G. Di, Fontananova, E. & Drioli, E. Energetics of protein nucleation on rough polymeric surfaces. *J. Phys. Chem. B* **114**, 13650–13655 (2010).

2. Lin, Y. *et al.* Self-assembled monolayer enables hole transport layer-free organic solar cells with 18% efficiency and improved operational stability. *ACS Energy Lett.* **5**, 2935–2944 (2020).

3. Farag, A. *et al.* Evaporated self-assembled monolayer hole transport layers: lossless interfaces in p-i-n perovskite solar cells. *Adv. Energy Mater.* **13**, 2203982 (2023).

4. Endres, J. *et al.* Valence and conduction band densities of states of metal halide perovskites: a combined experimental–theoretical study. *J. Phys. Chem. Lett.* **7**, 2722–2729 (2016).

5. Park, S. M. *et al.* Engineering ligand reactivity enables high-temperature operation of stable perovskite solar cells. *Science* **381**, 209–215 (2023).

6. Jiang, Q. *et al.* Surface reaction for efficient and stable inverted perovskite solar cells. *Nature* **611**, 278–283 (2022).

7. Chen, H. *et al.* Quantum-size-tuned heterostructures enable efficient and stable inverted perovskite solar cells. *Nat. Photonics* **16**, 352–358 (2022).

8. Chen, S., Xiao, X., Gu, H. & Huang, J. Iodine reduction for reproducible and high-performance perovskite solar cells and modules. *Sci. Adv.* **7**, 1–7 (2021).

9. Zheng, X. *et al.* Managing grains and interfaces via ligand anchoring enables 22.3%-efficiency inverted perovskite solar cells. *Nat. Energy* **5**, 131–140 (2020).

10. Peng, W. *et al.* Reducing nonradiative recombination in perovskite solar cells with a porous insulator contact. *Science* **379**, 683–690 (2023).

11. Wu, X. *et al.* Backbone engineering enables highly efficient polymer hole-transporting materials for inverted perovskite solar cells. *Adv. Mater.* **35**, 2208431 (2023).

12. Li, F. *et al.* Hydrogen-bond-bridged intermediate for perovskite solar cells with enhanced efficiency and stability. *Nat. Photonics* **17**, 478–484 (2023).

13. Shi, P. *et al.* Oriented nucleation in formamidinium perovskite for photovoltaics. *Nature* (2023) doi:10.1038/s41586-023-06208-z.

14. Zhao, X. *et al.* Accelerated aging of all-inorganic, interface-stabilized perovskite solar cells. *Science* **377**, 307–310 (2022).

15. Lin, Y.-H. *et al.* A piperidinium salt stabilizes efficient metal-halide perovskite solar cells. *Science* **369**, 96–102 (2020).

16. Yang, S. *et al.* Stabilizing halide perovskite surfaces for solar cell operation with wide-bandgap lead oxysalts. *Science* **365**, 473–478 (2019).